Engineering Fracture Mechanics 339 (2026) 112126

Contents lists available at ScienceDirect

Engineering Fracture Mechanics

journal homepage: www.elsevier.com/locate/engfracmech

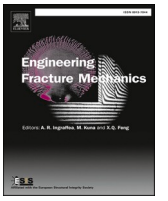

Study on the mechanical state of inner surface crack tips at SA508-52M-316L dissimilar metal welded joint interfaces

Shuai Wang [a,b], Yapeng Li [a], Bin Wang [b,*], Wanzhong Li [a], Lu Cui [a], Guiyi Wu [c], Lorna Anguilano [d], He Xue [e]

[a] School of Mechanical Engineering, Xi'an Shiyou University, Xi'an 710065, China
[b] Department of Mechanical and Aerospace Engineering, Brunel University of London, Uxbridge UB8 3PH, UK
[c] Centre of Excellence for Advanced Materials, Dongguan 523808, China
[d] Experimental Techniques Centre, Brunel University of London, Uxbridge UB8 3PH, UK
[e] School of Mechanical Engineering, Xi'an University of Science and Technology, Xi'an 710054, China

ARTICLE INFO

Keywords:
Dissimilar metal welded joints
Surface crack
Mechanical heterogeneity
Mechanical state on the crack tip

ABSTRACT

Low alloy steel SA508 welded to type 316L austenitic stainless steel using nickel-based filler materials, such as alloy 52M, represents one of the most frequently employed configurations of dissimilar metal welded joints (DMWJs) within the primary circuit of a pressurized water reactor (PWR). In response to the issue of structural integrity assessment of DMWJs at the primary circuit safe-end, a three-dimensional full-size finite element model considering the material property gradient was established. The mechanical response characteristics of inner surface crack tips under the coupling effects of complex loading and mechanical heterogeneity were systematically analyzed. By integrating sub-modeling techniques with the predefined field method, a multiscale correlation analysis between the global mechanical behavior of the full-size structure and the local stress–strain fields at crack tips was conducted. The influences of crack location on stress triaxiality and plastic strain distribution at crack tips were specifically investigated. A comparative analysis reveals that the conventional sandwich model underestimates crack-tip peak opening stress by approximately 15% at the SA508-52Mb interface and by about 11% at the 52Mw-316L interface within their respective heat-affected zones (HAZs); corresponding crack-tip peak plastic strain (PEEQ) is overestimated by roughly 13% and 46%. Analysis shows that crack-tip opening stress and plastic strain exhibit higher values in the SA508 and 316L HAZs. Furthermore, cracks near structural discontinuities demonstrate more pronounced mechanical heterogeneity than those in flat regions. The proposed continuous transition model effectively addresses this limitation, providing a more accurate mechanical assessment for engineering applications.

1. Introduction

In the primary circuit of a pressurized-water reactor (PWR), austenitic stainless steels and nickel-based alloys are widely used as key structural materials owing to their excellent mechanical properties in high-temperature and high-pressure water environment. In the type AP1000 nuclear power plant (NPP), the reactor pressure vessel (RPV) is fabricated from SA508 low-alloy steel, because of its

* Corresponding author at: School of Mechanical Engineering, Xi'an Shiyou University, Xi'an 710065, China.
E-mail address: bin.wang@brunel.ac.uk (B. Wang).

https://doi.org/10.1016/j.engfracmech.2026.112126
Received 26 December 2025; Received in revised form 24 March 2026; Accepted 1 April 2026
Available online 1 April 2026

Nomenclature

α	the yield offset coefficient
ν	Poisson's ratio
E	Young's modulus
hi	indentation depth
n	the strain hardening exponent
D	the distance
g	gravitational acceleration
ρ	material density
ε	strain
ε_e	elastic strain
ε_p	plastic strain
σ_y	yield strength
σ_b	tensile strength
σ_R	residual tensile stress
σ_m	the hydrostatic stress
σ_{eq}	the Von Mises equivalent stress
M	Bending moment
P_i	Internal pressure
P_a	Axial tensile load
F_{max}	maximum indentation load
h_r	residual indentation depth

Abbreviations

DMWJs	dissimilar metal welded joints
PWR	pressurized water reactor
NPP	nuclear power plant
RPV	reactor pressure vessel
SCC	stress corrosion cracking
FB	fusion boundary
HAZ	heat affected zone
FE-SEM	field emission scanning electron microscope
EBSD	electron backscatter diffraction
FE	Finite element
C3D8	8-node linear hexahedral element
FCC	face-centered cubic
IPF	inverse pole figure
IQ	image quality
BCC	body-centered cubic
WM	weld metal
PEEQ	equivalent plastic strain
SENB	single-edge notched bend specimen
EDI	Equivalent domain integral method

strength, good ductility, low cost, and good neutron irradiation resistance. The piping end is made of corrosion-resistant 316L austenitic stainless steel. The isolation layer and the butt weld are composed of nickel-based alloy 52M. The alloy 52M used for the RPV end is designated as 52Mb, while that used for the piping end is designated as 52Mw.

The SA508-52M-316L dissimilar metal welded joint (DMWJ), which comprises three distinct alloys with differing mechanical properties, harnesses the beneficial properties of each constituent to achieve superior combined performance. However, this joint has been found to be susceptible to stress corrosion cracking (SCC) in primary water systems, posing significant challenges to the structural integrity and safe operation of PWRs. Such degradation is particularly prone to occur in the fusion boundary (FB) and heat affected zone (HAZ) of the DMWJ.

Accurate assessment of the gradient in mechanical properties and the concomitant crack growth driving force at critical locations within the DMWJ is crucial for conducting structural integrity analyses of PWRs. The sandwich model has been utilized to assess the mechanical and fracture behavior of DMWJs. Several studies, including those by Qiang et al., and Zhang et al. have employed this model to characterize the mechanical properties of DMWJs. However, the simplified sandwich model does not account for variations in material properties within the HAZ and the FB of the joint [1,2]. For example, Wang et al. constructed a non-uniform mechanical property field coupled with a crack-growth criterion to reveal how cracks in dissimilar-metal welded joints deflect under the driving

influence of heterogeneous yield-strength fields and how the crack-tip field evolves. They report that the crack-tip driving force is larger on the high-yield-strength side. This makes cracks more likely to propagate toward that side, and that crack growth induces a redistribution of residual stress that also affects local strain rates [3]. Similarly, Wang et al. using microstructure and hardness distributions and implementing mechanical gradients in the weld with ABAQUS USDFLD, further confirmed that mechanical discontinuities at the interface are significant and can serve as potential sites for damage initiation. They showed that crack propagation is accompanied by a reorganization of the crack-tip field and by marked residual deformation, and they emphasized that crack assessment should be based on the local material properties in the region where the crack is located [4]. A broader theoretical review indicates that the driving force for SCC in DMWJs is controlled jointly by crack nucleation mechanisms, growth models, interfacial characteristics, and material resistance. Therefore, the coupling between mechanical loading and corrosive environment has therefore become a central difficulty in lifetime prediction for welded structures [5].

In the areas of crack-path prediction and crack-tip field simulation, modelling heterogeneity via material strength mismatch has become mainstream. Wang et al. combined the extended finite element method (XFEM) with a de-bonding approach to systematically predict crack propagation paths in DMWJs, showing that cracks tend to deflect toward regions of higher yield strength and that substantial residual stresses develop along the propagation path [6]. Bi et al., using a coupling of ABAQUS USDFLD and XFEM, reported that cracks are more likely to deflect toward the lower yield-strength side, illustrating a complex competition between yield-strength gradients and the direction of crack driving force [7]. Gong et al. conducted a leak-before-break (LBB) analysis for a nuclear RPV's DMWJ by developing a three-dimensional finite element (FE) model that incorporated the pipe-nozzle geometry and material inhomogeneity, analyzing crack growth stability at the A508/Alloy82 interface using the J-integral theory. Their study demonstrated that LBB assessment diagrams could effectively predict defect behavior under severe loads, showing that the safety margin (feasibility region) expands when the applied bending moment decreases or the material's crack growth resistance (J-R curve) increases [8]. Zhao et al. proposed a constraint parameter, Dp, integrating both in-plane and out-of-plane constraints based on the PEEQ gradient ahead of the crack front in DMWJs. Using the USDFLD subroutine for continuous property transition and the sub-model technique for detailed constraint analysis, they found that center cracks exhibit higher propagation potential than surface cracks, with the SA508/52 Mb interface being the most critical location [9]. Gu et al. studied the fracture behavior of nuclear safety-end DMWJs by numerically introducing localized residual stresses into single-edge notched bend (SENB) specimens using a pre-loading and restart simulation method. Their findings indicated that tensile residual stresses, induced by pre-loading on one side, reduced the J-R curve, whereas compressive residual stresses from the opposite side increased it [10]. Okonkwo et al. employed electron back-scattered diffraction (EBSD) to analyze the grain size across the refined, partially refined, and base metal (BM) matrix regions within the HAZ of an SA508-309 L/308 L DMWJ. The yield strength of the HAZ was subsequently determined using the Hall-Petch correlation derived from the grain size data. Nevertheless, the predictive capability of this EBSD-based approach calls for further experimental verification to confirm its reliability across different DMWJ conditions [11]. From the viewpoints of microstructure and corrosion, Dong et al. analyzed EAC behavior on DMWJs and found that the dilution zone grain boundaries are more susceptible to cracking: strength mismatch and galvanic corrosion can promote interfacial crack initiation under normal loading, while concurrent oxidation can inhibit through-thickness crack propagation and thereby significantly reduce crack-tip stress/strain [12,13]. At the more macroscopic level of structural-integrity analysis, Wang et al. used elastoplastic finite-element modelling together with crack-growth experiments to show that initial crack morphology critically influences the transition from semi-through-thickness to through-thickness propagation, and that the distribution of the J-integral maximum along the crack front evolves with crack shape – an important finding for integrity assessment of surface-cracked structures [14]. Peng et al. proposed a crack-path prediction method based on the maximum principal stress criterion combined with element-deletion strategies and a bio-evolutionary optimization scheme, demonstrating effectiveness for life prediction of complex aerospace structures [15]. Earlier, Xue et al. coupled a film-slip-dissolution/oxidation model with elastoplastic finite-element analysis and experimental data to provide a useful framework for estimating EAC propagation in light-water reactor components, with clear application value for pre-test analyses of non-standard specimens [16].

Overall, existing research has made substantial advances in microstructural characterization, mechanical-heterogeneity analysis, environment-coupled behavior, and numerical simulation techniques, progressively forming an integrated multi-scale framework that spans microstructure characterization, local mechanical-field analysis, crack-path prediction, and structural-integrity assessment. Nevertheless, a key challenge remains the quantitative characterization of the mechanical state at the crack tip under environmental influences. This study elucidated the origins of mechanical inhomogeneity and identified crack-sensitive zones in safe-end DMWJs through microstructural analysis. Subsequently, a full-scale 3D FE model, which incorporated complex operational conditions via the sub-modeling technique and a predefined temperature field, was developed. This comprehensive approach enabled an evaluation of the crack-front mechanical states (stress, strain, and local stress triaxiality) for internal surface cracks at various locations, thereby providing an analysis of their potential propagation directions.

2. Experiments

2.1. Materials and specimen

A DMWJ composed of SA508-52M-316L was selected as the research object. A full-scale mock-up of DMWJ used in type AP1000 PWRs is shown in Fig. 1(a). The structure primarily consists of 316L stainless steel at the piping end, known for its excellent corrosion resistance, and SA508 alloy steel as the base material at the pressure vessel end [17]. The weld metal (WM) employs nickel-base Alloy 52M, where the specific alloy used on the pressure vessel side (SA508 side) is designated as 52Mb, and the alloy used on the piping side (316L side) is designated as 52Mw in the DMWJ. The wording has been corrected as suggested. Connecting different types of metallic

materials by welding enables the full utilization of each material's performance advantages under specific operating conditions, thereby enhancing the overall service life of NPPs. The specimen (SA508-52M-316L) used for indentation test in this work was extracted from an actual DMWJ. The cutting position (gray dashed rectangle) and specimen are shown in Fig. 1(b) and (c), respectively.

2.2. Indentation test

Because of the apparent mechanical heterogeneity present in DMWJ, conventional uniaxial tensile testing cannot accurately determine the mechanical properties. Therefore, we employed a custom-developed indentation testing apparatus to inversely determine the mechanical property distribution in the welded joint region through indentation experiments. The quasi-static indentation behavior was evaluated using a UTM-6103 universal testing machine. The system was fitted with a 0.5 mm radius spherical indenter fabricated from tungsten carbide to ensure rigidity. Tests were carried out under displacement control, with the indenter advancing at a constant rate of 0.1 mm/min until achieving a penetration depth of 0.1 mm. To ensure experimental consistency, the ambient temperature was strictly monitored, and its variation was maintained below 0.2°C per hour throughout all tests. In accordance with the relevant requirements for indentation testing specified in GB/T 22458–2008, the distance between indentation locations was set to 2 mm [18]. Additionally, to increase the number of test points, a staggered distribution pattern with two sets of test points was employed to enhance the density of measurement points. The distance between these two sets of test points was set to 5 mm. The specific indentation locations ultimately determined for the welded specimen are illustrated in Fig. 2, with a total of 49 measurement points established. The distribution of test points was empirically determined according to the microstructure analysis of the DMWJ. Points were systematically located to cover all key regions: the BM, WM, and the HAZ. The method for obtaining the mechanical property parameters of the DMWJ material via indentation testing is as follows. First, based on the Hollomon model, a FE method is employed to establish the correlation between indentation parameters (maximum indentation load F_{max} and residual indentation depth h_r) and material mechanical property parameters (yield strength σ_y and strain-hardening exponent n). Subsequently, indentation tests are performed on the DMWJ to acquire the indentation test parameters in the direction perpendicular to the welded line. Finally, based on the relationship between the indentation parameters and the material mechanical property parameters, the indentation test data obtained perpendicular to the weld direction on the DMWJ are converted into the corresponding mechanical property parameters. For detailed procedures on obtaining mechanical properties of DMWJs through indentation experiments, refer to Reference [19].

2.3. Microstructure analysis

The distribution of major alloying elements across the fusion line interface of SA508-52Mb was analyzed using a ZEISS SUPRA 35VP high-resolution field emission scanning electron microscope (FE-SEM) equipped with an EDAX energy dispersive spectroscopy

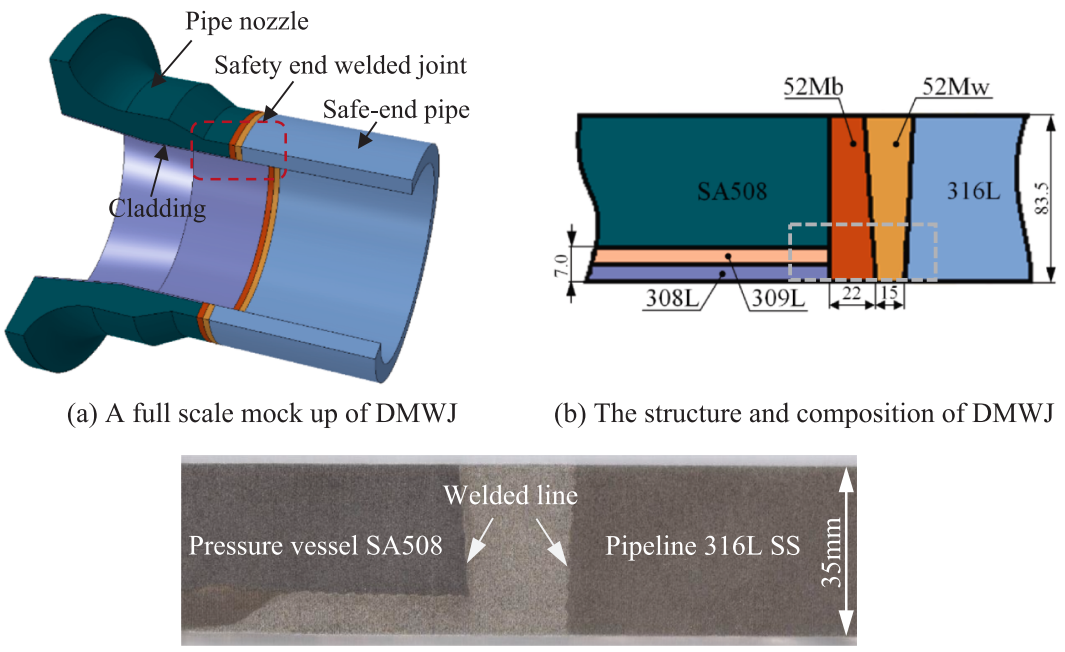

(a) A full scale mock up of DMWJ

(b) The structure and composition of DMWJ

(c) DMWJ specimen (thickness 15mm)

Fig. 1. Typical DMWJ structure for connecting the pipe nozzle of a RPV to the safe-end pipe.

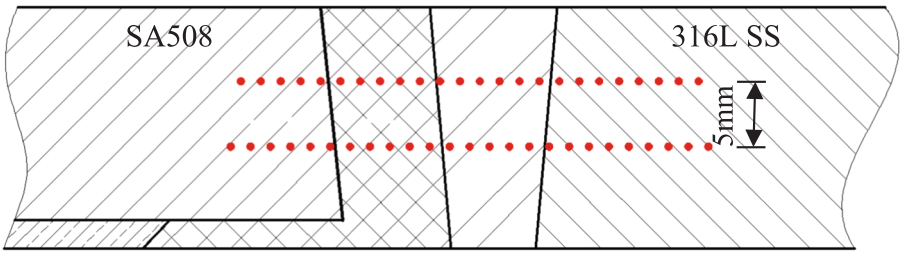

Fig. 2. Indentation test area.

system. To enhance analytical accuracy, the specimen surface required meticulous preparation. Welded samples were sequentially ground with 240# to 2000# SiC abrasive papers under water lubrication, followed by final polishing with a 0.25 μm colloidal silica suspension until all mechanical scratches were eliminated prior to microscopic examination.

Specialized software was employed to statistically quantify the distribution and proportional fractions of microstructural constituents within the DMWJ. Concurrently, electron backscatter diffraction (EBSD) was utilized to characterize grain orientations, phase distributions, and residual strain patterns (KAM) in both the BM and weld zones adjacent to interfacial regions. The EBSD scanning locations were divided into three regions, as indicated by the red, green, and blue boxes in Fig. 3, representing the fusion line at the SA508-52Mb interface, the fusion line at the 52Mw-316L interface, and the 316L stainless steel region on the piping end, respectively. Instrument control and data analysis were performed using ZEISS Smart SEM and TSL OIM Analysis 7 software platforms, respectively.

3. Finite element model analysis

3.1. Constitutive model

Due to the limitation of the HAZ size, it is difficult to cut standard tensile specimens from the SA508-52M-316L DMWJ. Consequently, indentation testing serves as a prevalent technique for assessing mechanical properties, particularly within local FB regions of a material that exhibit gradients or variations in mechanical behavior. The constitutive model used in this study for determining the mechanical properties of the DMWJ is based on the calculation method established in our research group's prior work, and the method can obtain the mechanical parameters distribution of the welded joint [19]. The yield stress and hardening exponent distribution for SA508-52M-316L DMWJ are shown in Figs. 4 and 5, respectively.

The relationship between the yield stress σ_y, the strain hardening exponent (n) and the distance (D) near the weld for SA508, the 316L heat-affected zone (HAZ), and the weld metals 52Mb and 52Mw were fitted using the Curve Fitting Toolbox application within MATLAB software. The fitting equations and their corresponding goodness-of-fit statistics are outlined below:

For the interface location between the SA508 heat-affected zone and the weld metal 52 Mb:

$\sigma_y = 0.698D^3 - 4.946D^2 - 6.244D + 431.2$, $R^2 = 0.8223$ (1)

$n = -2.539 \times 10^{-5}D^3 + 4.116 \times 10^{-4}D^2 - 8.18 \times 10^{-4}D + 0.101$, $R^2 = 0.8702$ (2)

For the interface location between the weld metal 52Mw and the 316L heat-affected zone:

$\sigma_y = -8.443 \times 10^{-3}D^3 - 0.3605D^2 + 28.12D + 46.66$, $R^2 = 0.8262$ (3)

$n = -5.669 \times 10^{-6}D^3 - 4.956 \times 10^{-4}D^2 - 0.0128D + 0.205$, $R^2 = 0.9092$ (4)

The Young's modulus for the SA508, 52M and 316L SS are 202.41 GPa, 178.13 GPa and 196 GPa, respectively [20–22]. The continuous variation of mechanical properties was considered in this study, and the material model for the DMWJ with continuous transition mechanical property (i.e. continuous model) was built by using a predefined temperature field method.

The sandwich model is a widely used material model to characterize welded joints mechanical performance. The sandwich model for DMWJ was partitioned, with different materials assigned different σ_y and n, and the mechanical property of the HAZ metal is assumed to be the same as the BM in this simplification. In this work, for comparison purposes, the Mises stress and equivalent plastic strain (PEEQ) along the crack tip from sandwich model and continuous model were analyzed with the same FE model simultaneously.

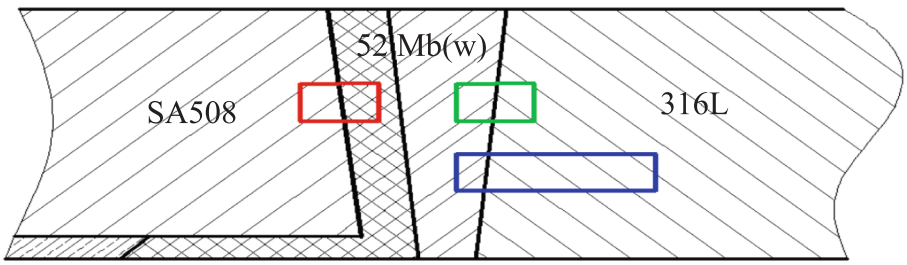

Fig. 3. EBSD scanning area.

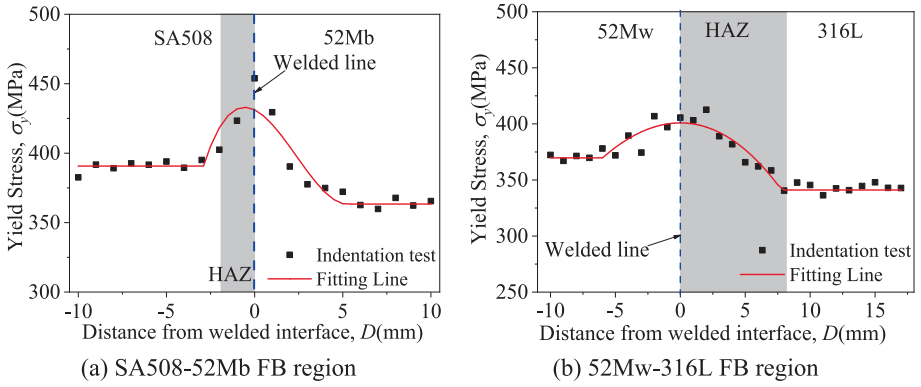

Fig. 4. Yield stress distribution in the FB region in the SA508-52M-316L DMWJ.

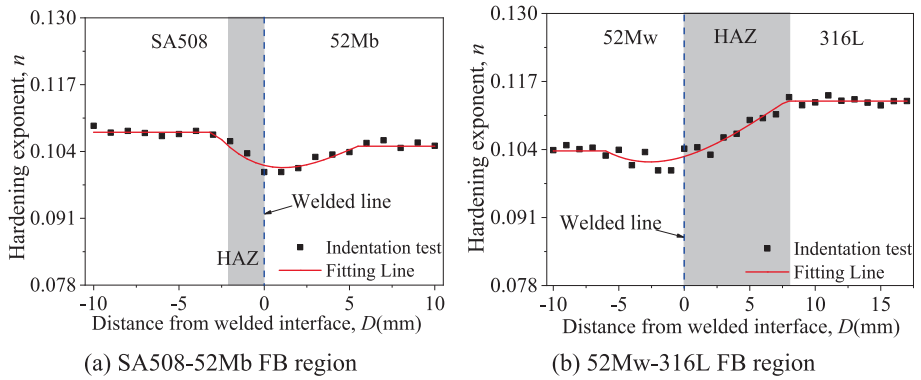

Fig. 5. Hardening exponent distribution in the FB region in the SA508-52M-316L DMWJ.

The mechanical parameters of the four materials used in the sandwich material model are presented in Table 1[23].

3.2. Geometric model

Referring to the design standards of the third-generation PWR NPPs such as the AP1000 in China, the schematic diagram of the welded joint area at the RPV nozzle safe-end and primary loop pipeline is shown in Fig. 6, with dimensions in millimeters (mm) [24,25]. The left side of the weld joint is connected to the RPV, the right side to the primary loop main pipe, and the intermediate area adopts dissimilar metal welding. The angles between the BM and the WM, measured as approximately 85° for the SA508-52Mb weld and 86° for the 52Mw-316L weld relative to the horizontal direction, are nearly perpendicular to the pipe axis. In this study, the geometry was simplified by setting this interface angle to 90° for analytical clarity.

As shown in Fig. 7, to study the stress–strain fields around inner surface cracks at these critical locations, axial elliptical inner surface cracks with $d = 2$ mm and $c = 4$ mm were placed at the SA508-52Mb interface and the 52Mw-316L interface, respectively. It should be noted that, due to its relatively small thickness (7 mm), the 309 L/308 L stainless steel cladding was excluded from the subsequent numerical model for the sake of analytical simplification.

The full-scale global three-dimensional model of the safety end DMWJ, as shown in Fig. 4(a), is established. To improve the accuracy of the analysis results for inner surface cracks, reduce computation time, and enhance computational efficiency, sub-modeling techniques based on ABAQUS are employed.

Sub-models are established at the SA508-52Mb interface, 52Mw-316L interface, and the 316L pipe location near the inner wall,

Table 1
The mechanical parameters for the sandwich model.

Material	Young's modulus, E/MPa	Yield stress,σ_y/MPa	Hardening exponent, n
SA508	202,410	382.6	0.1090
52Mb	178,130	377.8	0.1032
52Mw	178,130	385.9	0.1020
316L	196,000	340.7	0.1134

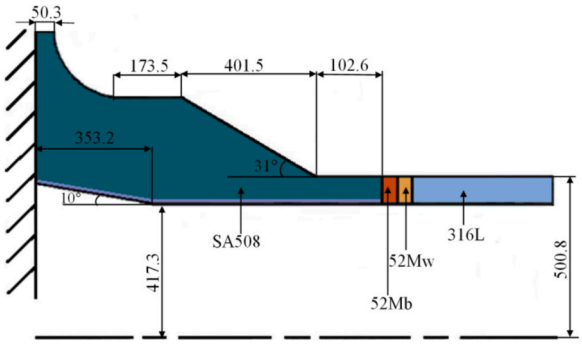

Fig. 6. The dimensional parameters of DMWJs for nuclear power safety ends.

with specific dimensions of 18 mm × 9 mm × 20 mm. Additionally, to more precisely obtain the stress–strain distribution at the crack tip of the inner surface crack, the position at the crack tip is extracted and treated as a secondary sub-model for computation. The extraction locations and shapes of the sub-model and secondary sub-model are shown in Fig. 8(b) and (c), respectively.

According to literature, the load on the safe-end DMWJ during service is mainly composed of bending moment, internal pressure, and self-weight of the pipe. Among them, the bending moment under actual service conditions of the DMWJ is also considered [26]. The inclusion of a bending moment, superimposed on the axial tension, is intended to replicate a multiaxial service load state. Although the bending-induced stress is primarily axial relative to the crack, it does not directly contribute to a pure Mode I crack-tip opening. Its key role is in redistributing the through-thickness stress field and accelerating plastic yielding of the remaining ligament, thereby dictating the plastic collapse limit state, especially for deeper flaws. The working loads of the safe-end DMWJ under service conditions are listed in Table 2.

For the global model, since the pipe end is rigidly connected to the RPV in reality, a fixed constraint was applied to the left end. As a half-model was used for calculation, symmetric boundary conditions were applied to the symmetric plane.

External loads were applied as follows: an axial tensile load was applied to the right end based on Table 2 parameters; a bending moment was applied through a reference point at the pipe center; and the working pressure due to the high-temperature water environment was applied as internal pressure on the inner wall. The boundary conditions for the global model, sub-model, and second sub-model are shown in Fig. 9 (a), (b), and (c), respectively.

In accordance with ABAQUS sub-model techniques, boundary conditions of sub-model and second sub-model were driven by the results obtained from upper-level models. Moreover, considering the large geometrical size and metallic nature of the welded structure, the self-weight effect could not be neglected. Therefore, gravitational acceleration $g = 9.8 \times 10^3$ mm/s^{2}and material density $\rho = 7.85 \times 10^{-9}$ tonne/mm^3 were applied to the models [28].

3.3. The mesh and element choice

In this study, an 8-node linear hexahedral element (C3D8) was employed to construct the global model and the sub-model systems, ensuring consistent element types while maintaining computational efficiency. The significant stress gradients generated by stress concentration at the crack tip prompted the implementation of a localized mesh refinement strategy. This was achieved by strategically controlling the “seed” density to deploy a fine mesh around the crack tip front, with coarser meshes maintained in non-critical areas. The FE meshes of the global model, sub-model, and second sub-model are shown in Fig. 9.

The final global model, sub-model, and secondary sub-model contained 133,960, 36,176, and 76,464 elements, respectively. Sensitivity verification of the FE mesh was accomplished through multiple attempts with different grid types and quantities, balancing computational time with accuracy. The mesh model with good mesh quality and no distortion observed in the transition regions.

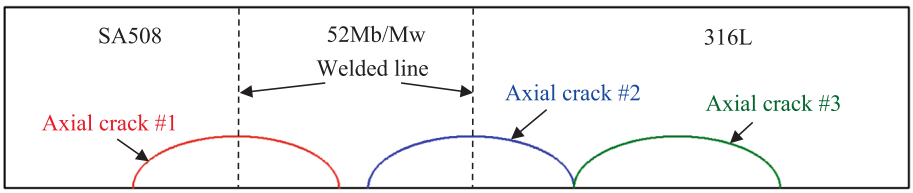

Fig. 7. Schematic diagram of the position of the inner surface crack in the weld joint.

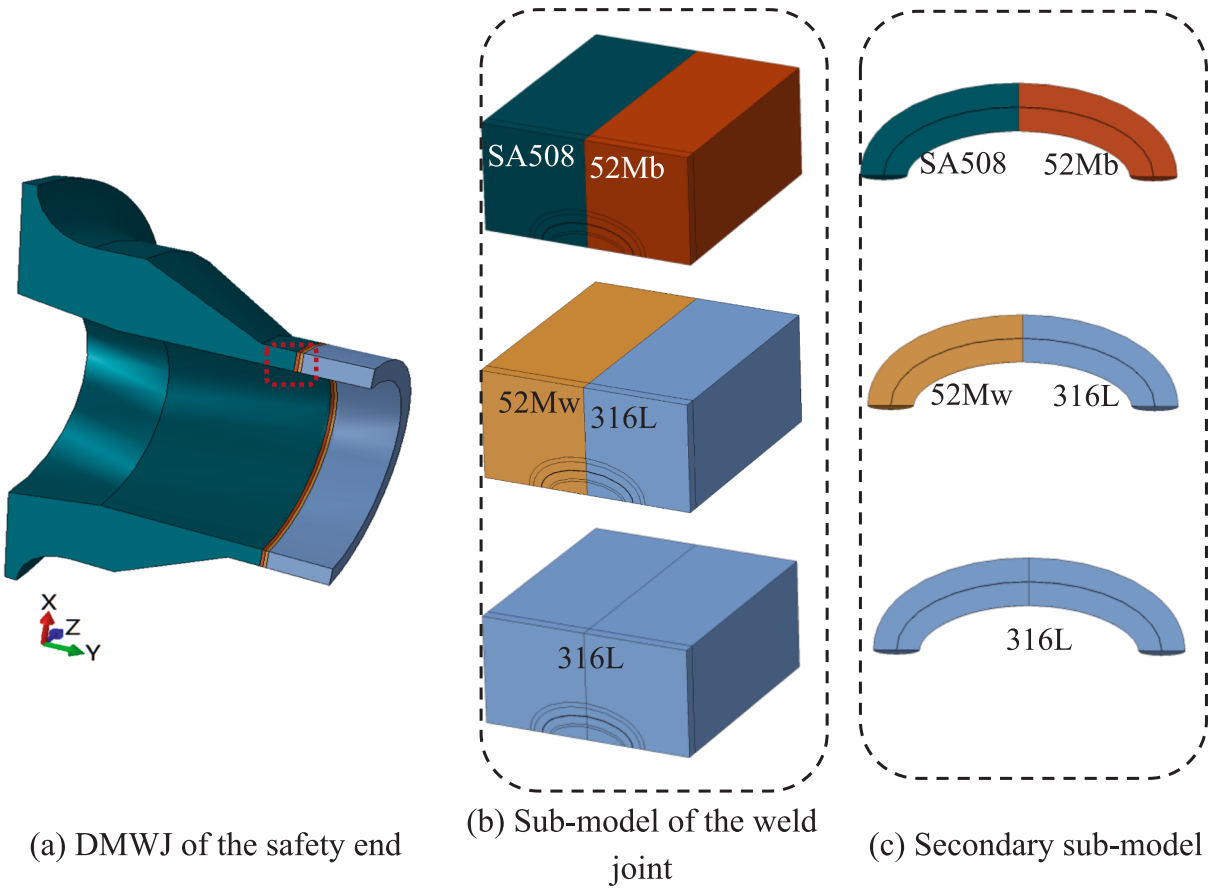

Fig. 8. Three-dimensional model of the nuclear power safety end DMWJ.

Table 2
Working loads of the nuclear power safety end DMWJ [27].

Bending moment, M (N·mm)	Axial tensile load, P_a (MPa)	Internal pressure, P_i (MPa)
2.492×10^9	44	17

4. Results and discussion

4.1. Microstructure analysis

4.1.1. EBSD results of the 52Mw-316L interface area

The detailed EBSD analysis results of the interfacial region in the 52Mw-316L welded joint are illustrated in Fig. 10. The grain orientation outside the fusion boundary is perpendicular to the direction of the weld pool boundary, primarily due to the maximum temperature gradient and faster heat dissipation in this direction. Regarding phase distribution, this region exhibits uniformity because both the nickel-based 52M alloy and 316L stainless steel possess an austenitic structure (as shown in the phase distribution map in Fig. 10(b)), sharing the same face-centered cubic (FCC) crystal structure. Fig. 10(c) presents the inverse pole figure (IPF) map of the investigated region, illustrating the crystallographic orientation distribution. Accelerated grain growth is observed when the crystallographic orientation aligns with the maximum temperature gradient direction. This preferential growth results in the development of coarse columnar dendritic structures, as evidenced on the left side of Fig. 10(c).

Fig. 10(d) presents the analytical results of residual strain distribution within the welded joint. A significant concentration of residual strain is evident adjacent to the weld fusion line, particularly on the 316L stainless steel side. This strain localization is predominantly attributed to the severe thermomechanical cycling experienced in this region, characterized by rapid heating/cooling rates and high peak temperatures during the welding process. The pronounced “thermal expansion–contraction effect” following weld solidification induces considerable residual stress/strain due to constrained shrinkage.

As the distance from the fusion line increases, a corresponding decline in both the peak temperature and the thermal gradient

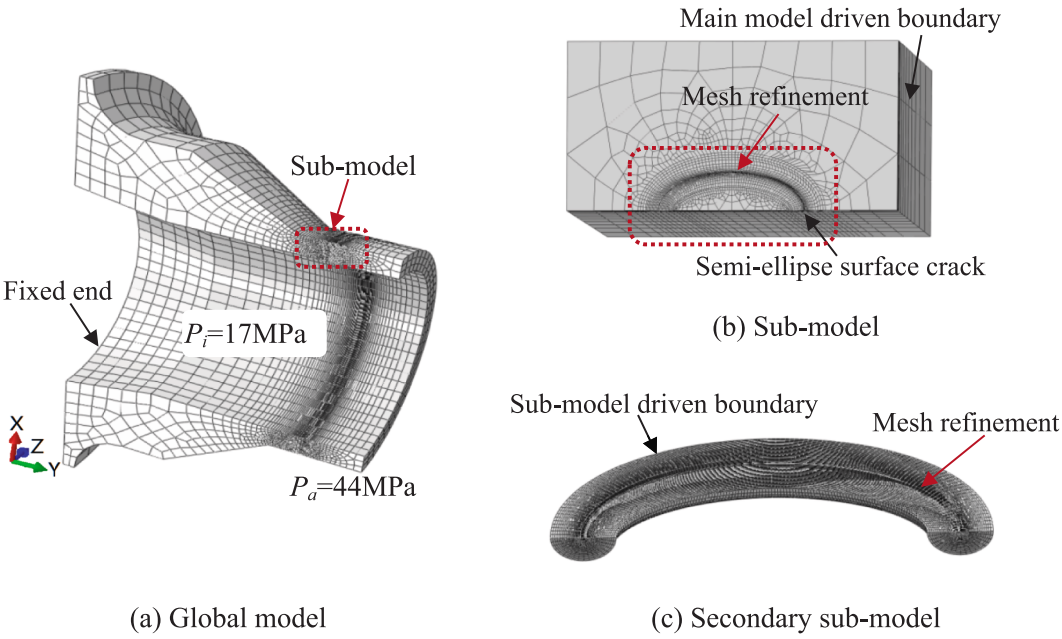

Fig. 9. Finite element mesh model of the nuclear PWR primary loop weld joint.

during cycling is observed, resulting in a gradual attenuation of the residual strain magnitude on the 316L stainless steel side. Extensive literature has confirmed that elevated welding residual stress/strain accelerates the initiation of SCC and promotes its propagation [29,30]. The significant residual strain present within the HAZ of the 316L stainless steel, particularly at the interfacial region with the 52Mw material, creates a local condition of pronounced susceptibility to SCC.

4.1.2. EBSD results of the SA508-52Mb interface area

The EBSD analysis of the SA508-52Mb interfacial region is presented in Fig. 11(a). The image quality (IQ) map reveals a gray zone adjacent to the welded line, approximately 25 μm wide, formed due to dilution effects. The phase analysis in Fig. 11(b) indicates that the SA508 side exhibits a body-centered cubic (BCC) crystal structure, consistent with the tempered bainite microstructure typical of SA508 low-alloy steel. Fig. 11(c) displays the inverse pole figure (IPF) map, where no Type-II grain boundaries (sensitive to SCC) are detected.

The residual strain measurements are presented in Fig. 11(d). Residual strain predominantly concentrates on the SA508 alloy steel side, though its magnitude is lower than that observed in the 316L HAZ adjacent to the weld interface in Fig. 10. The nickel-based 52Mb alloy exhibits relatively minor residual strain with non-uniform distribution. Notably, residual strain is lower within the dilution zone but significantly higher near the WM interface. This substantial disparity in residual strain distribution across the weld interface increases susceptibility to SCC in this region.

The utilization of EBSD elucidated the reasons for the abrupt changes in mechanical properties of the material surrounding the weld from a microstructural perspective, which also provided guidance for determining crack locations in subsequent FE analysis.

4.2. The mechanical state along the front of an elliptical crack

Mechanical state parameters, such as crack-tip opening stress and PEEQ, can be directly incorporated into mechanistically based SCC growth rate models like the Ford-Andresen (F-A) model [31–33]. In such frameworks, the crack-tip strain rate, commonly obtained from plastic strain, along with the local stress state as characterized by stress triaxiality and opening stress, act as key drivers for crack propagation. Mapping these parameters along the crack front across different microstructural zones of the DMWJ enables the prediction of location-dependent SCC growth rates. This approach provides a quantitative means to assess the influence of mechanical heterogeneity on crack progression, identifying, for example, whether cracking accelerates within the HAZ or the WM. The mechanical parameters at the crack tips of elliptical internal surface cracks located at different positions are analyzed below.

4.2.1. The mechanical state at crack tip in the SA508-52 Mb interface

For the axial crack located at the SA508-52 Mb interface (Crack #1 in Fig. 7), Fig. 12 compares the crack front opening stress distributions calculated by two models: the sandwich model and the continuous transition model. Results indicate that the opening stress is higher on the SA508 side, compared to the 52Mb side, is due to the higher yield strength and hardening exponent of the SA508 base material. At the weld interface, the sandwich model (Fig. 12a) exhibited stress discontinuities, whereas the continuous transition model (Fig. 12b) exhibited smooth transitions, which better reflect the actual physical behavior. Notably, in regions remote from the

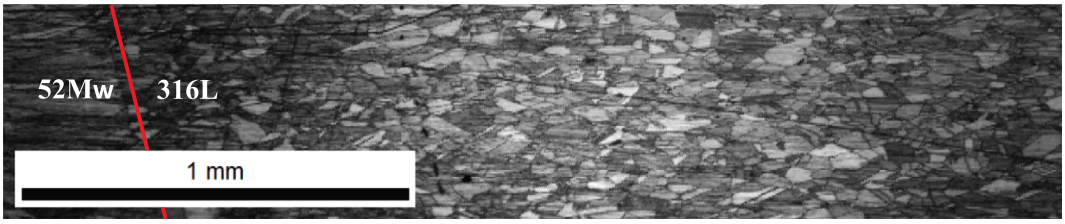

(a) Phase distribution map

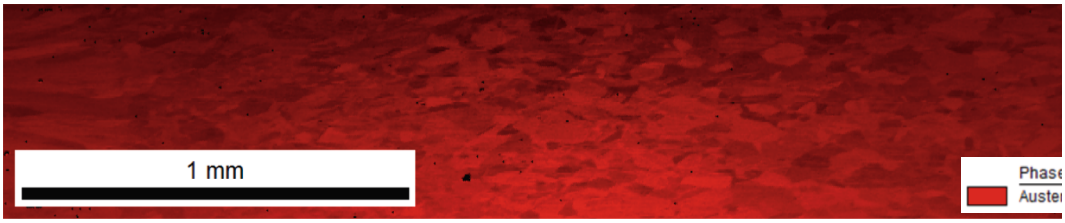

(b) Phase distribution map

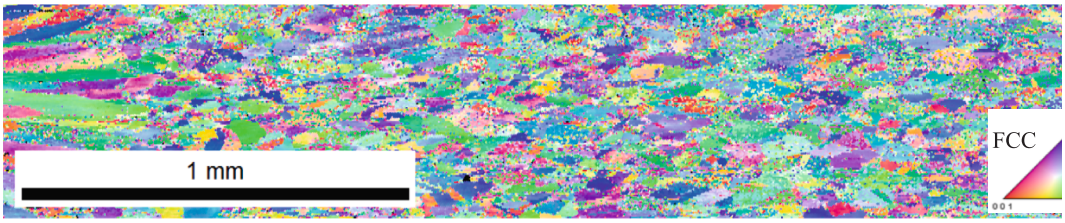

(c) Inverse pole figures (IPF)

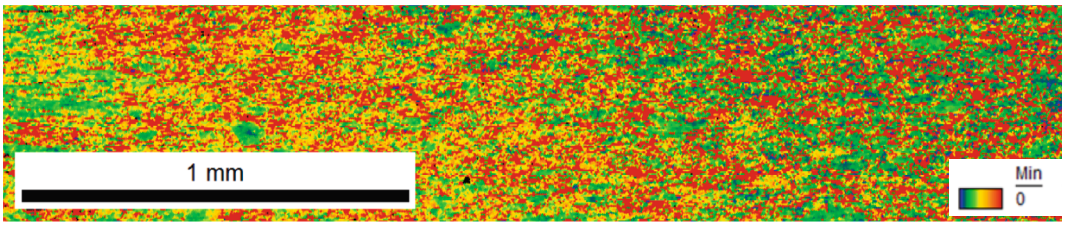

(d) KAM map

Fig. 10. EBSD analysis results of the interfacial region in the 52Mw-316L welded joint.

welded line, the results produced by both models are nearly identical.

To quantitatively analyze the distribution of opening stress and PEEQ along the crack front, data were extracted at a fixed distance of $r = 30$ μm from the crack tip and are presented in Fig. 13. The results indicate that the opening stress at the crack tip on the SA508 side is significantly higher than that on the 52Mb side, which is consistent with the contour plots. A corresponding distribution is observed for the PEEQ, with higher strain levels on the SA508 side.

Extensive studies have indicated that a material's lower resistance to plastic deformation readily induces elevated opening stress at the crack tip. This heightened opening stress, in turn, facilitates the initiation and propagation of SCC. For internal surface cracks situated at the SA508-52Mb interface, the opening stress at the deepest point of the crack is significantly greater than those at regions near the crack mouths (i.e., the sides of the crack). This disparity suggests that such cracks are more prone to extend in the depth direction. Furthermore, the higher crack-tip opening stress and PEEQ on the SA508 HAZ side indicate a stronger mechanical driving force for propagation toward this region compared to the 52Mb side. Consequently, an internal surface crack traversing the SA508-52Mb weld line may be more likely to grow toward the SA508 HAZ during depth-wise propagation, provided that the fracture toughness does not exhibit a strongly contrasting trend that could offset this driving force.

As shown in Fig. 13(a), the sandwich model exhibits a discontinuity in the opening stress within the weld region; a similar discontinuous phenomenon is also observed in the PEEQ distribution in Fig. 13(b). Although the distribution trends of the opening stress and PEEQ on both sides of the weld obtained by the sandwich model and the continuous transition model are generally consistent, the former significantly underestimates the opening stress while overestimating the PEEQ. A comparative analysis of the opening stress and PEEQ calculated by the two models indicates that, relative to the continuous transition model, the sandwich model

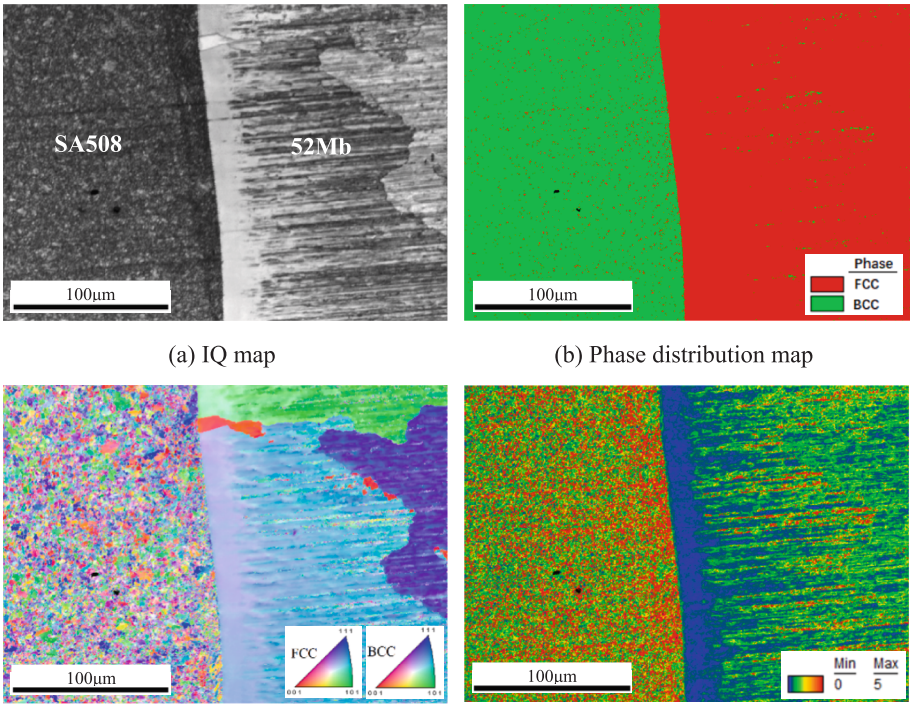

Fig. 11. EBSD analysis results of the interfacial region in the SA508-52 Mb welded joint.

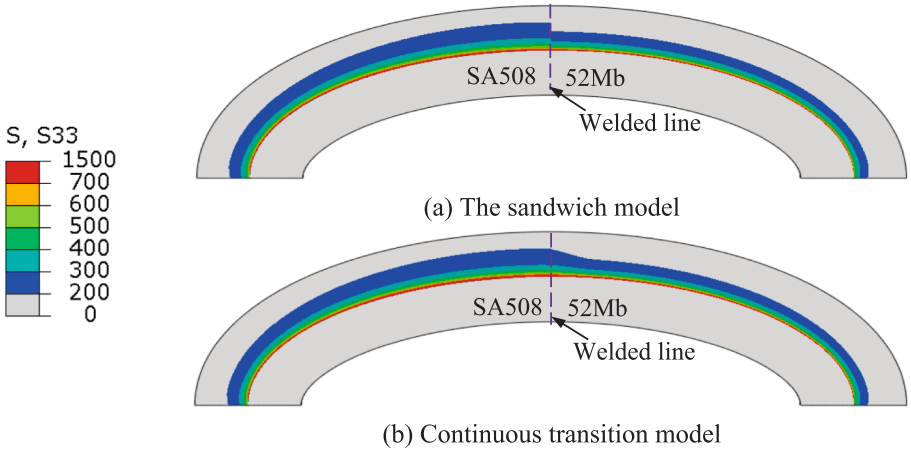

Fig. 12. Stress distribution of crack tip opening in the inner surface of SA508-52 Mb interface.

underestimates the crack-tip opening stress by approximately 15% and overestimates the PEEQ by about 13%. These discrepancies mainly occur within the HAZ of the SA508 BM and in the region adjacent to the weld on the 52Mb side. These areas are characterized by a steep gradient in material mechanical properties, which the sandwich model fails to accurately capture. This deviation is attributed to the fact that the continuous transition model adequately accounts for the gradual variation of material properties induced by the welding process in the transition zone, an effect neglected by the sandwich model.

4.2.2. The mechanical state at crack tip in the 52Mw-316L interface

For the axial crack #2 located at the 52Mw-316L interface, Fig. 14 compares the crack front opening stress distributions calculated by the two models. The results show that the opening stress on the 316L side is significantly higher than that on the 52Mw side, which is closely related to the differences in the mechanical properties of the base materials. At the weld interface, the sandwich model (Fig. 14a) still exhibits a stress discontinuity, whereas the continuous transition model (Fig. 14b) maintains a smooth stress transition.

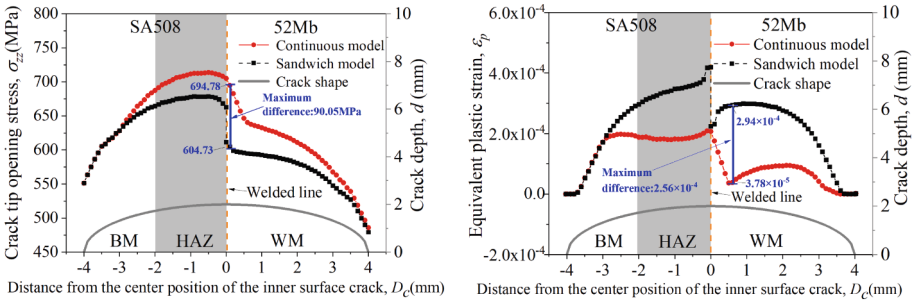

(a) Crack tip opening stress distribution (b) Equivalent plastic strain distribution

Fig. 13. Stress and strain distribution of internal surface cracks in SA508-52 Mb interface.

Similar to the case shown in Fig. 12, the results of the two models tend to converge in regions far from the welded line.

As shown in Fig. 15(a) and (b), the opening stress at the crack front on the HAZ of 316Lside is significantly higher than that on the 52Mw side, with the PEEQ distribution following a similar trend. For the elliptical inner surface crack at the 52Mw-316L interface, both the opening stress and PEEQ at the deepest point of the crack are greater than those near the surface regions (crack tips), indicating a higher propensity for crack propagation along the depth direction. Moreover, the stronger mechanical response (e.g., higher crack-tip opening stress) on the 316L side suggests a greater driving force for crack extension toward its adjacent HAZ. Consequently, a surface crack traversing the weld line may exhibit a propensity to deviate into the 316L HAZ, unless counteracted by a significantly higher fracture toughness in that region.

In Fig. 15, the sandwich model clearly displays discontinuities in both opening stress and PEEQ at the 52Mw-316L interface, a phenomenon consistent with the stress contour in Fig. 14. It is noteworthy that this discontinuity is more pronounced at the SA508-52Mb interface compared to the 52Mw-316L interface. In terms of distribution trends, the sandwich model and the continuous transition model yield generally consistent profiles of opening stress and PEEQ on both sides of the interface crack. However, the sandwich model underestimates the crack-tip opening stress by approximately 11% and overestimates the PEEQ value by about 46%, relative to the continuous transition model on the 52Mw-316L interface. This discrepancy is particularly evident in the HAZ of the 316L BM. Therefore, in structural integrity assessments of such welded joints, it is essential to account for the significant influence of the material property gradient in the HAZ on the crack-tip stress and strain fields.

4.2.3. The mechanical state at crack tip in the 316L HAZ and BM

For the axial crack #3 located on the inner wall of the 316L pipe, Fig. 16 presents a comparison showing that the opening stress along the crack front exhibits a uniform distribution, with the maximum stress concentrated at the deepest point of the crack, in contrast to the stress gradient characteristics observed in cracks at the weld interface. It is noteworthy that under this condition, there is no significant difference between the predictions of the sandwich model and the continuous transition model. However, detailed local stress–strain analyses at the crack tip are still necessary to further validate the applicability of the models.

The opening stress and PEEQ at a distance of 30 μm from the crack front were extracted from the computational results of the continuous transition model and the sandwich model for analysis. The results are shown in Fig. 17(a) and Fig. 17(b), respectively.

The distribution of opening stress in Fig. 17(a) exhibiting an “M”-shaped profile. Both the opening stress and PEEQ at the crack

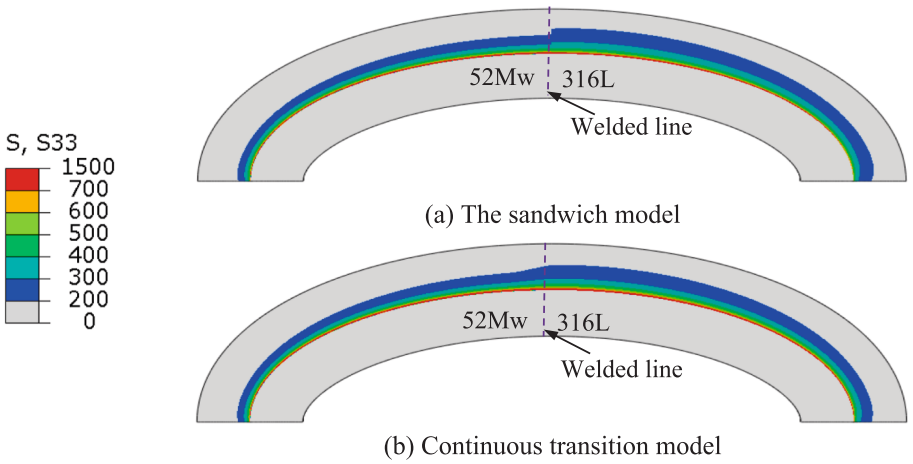

Fig. 14. Distribution of tensile stress at the crack tip of 52Mw-316L interface inner surface.

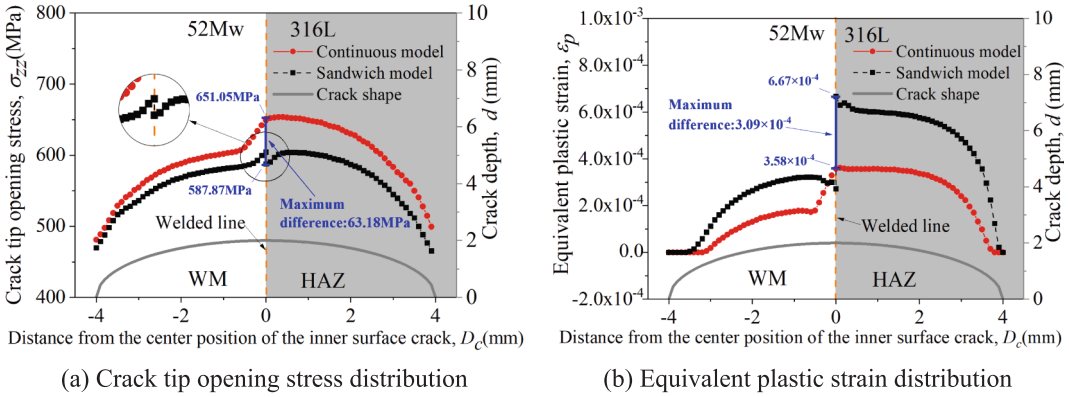

(a) Crack tip opening stress distribution (b) Equivalent plastic strain distribution

Fig. 15. Stress and strain distribution of internal surface cracks in 52Mw-316L interface.

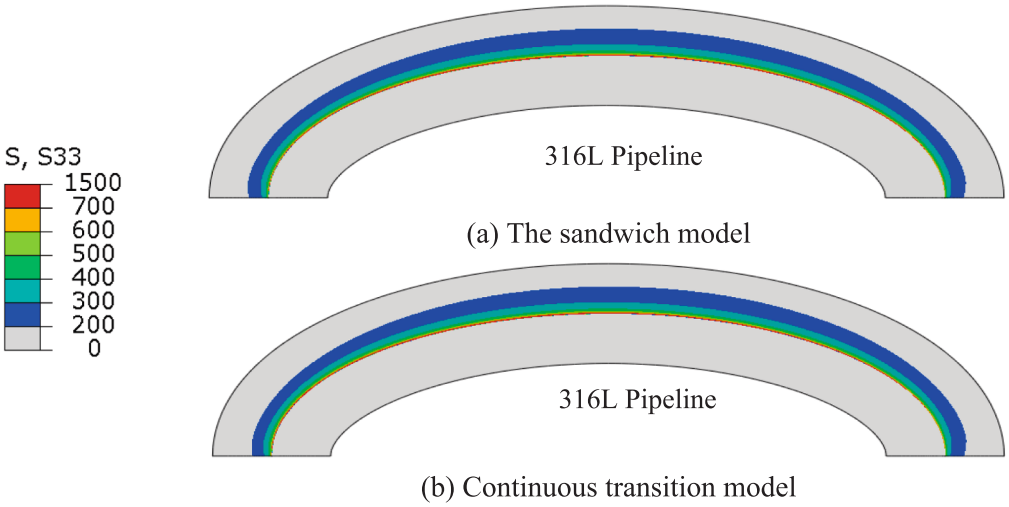

Fig. 16. Distribution of tensile stress at the crack tip of 316L pipeline interface inner surface.

depth are higher than those at the regions near the crack surfaces (both sides of the crack). As shown in Fig. 17, the crack opening stress and PEEQ obtained by the sandwich model exhibit essentially symmetric distributions. This is primarily because the sandwich model, when calculating the stress and strain fields at the tip of the inner surface crack in the pipeline, does not account for the presence of the HAZ, and the material at the crack location is assigned identical mechanical properties. In contrast, the continuous transition model considers the variation in mechanical properties within the HAZ, thereby providing a more accurate representation of the stress and strain variations for a crack located within the HAZ. In the 316L pipeline, the sandwich model underestimates the crack-tip opening stress by approximately 10% at the near-surface location of the crack within the 316L HAZ, while significantly overestimating the PEEQ value, relative to the continuous transition model. Consequently, when assessing the propagation behavior of cracks in pipelines near welds or within the HAZ, it is essential to fully consider the continuous gradient of mechanical properties in the weld and HAZ.

4.3. The effect of crack position on the stress triaxiality at the front edge of the crack

For thin-walled structures or specimens with small thickness, the stress state at the crack tip can be described using a plane stress condition, as the mechanical state at the crack tip region does not exhibit triaxial constraint. Numerous studies have shown that the triaxiality of stress at the crack tip significantly influences the fracture behavior of materials. Therefore, for the full-size safety-end welded joints subjected to various working loads, as investigated in this chapter, a detailed analysis of the triaxial constraint state at the crack front position is required.

The triaxiality of stress at the crack tip region is defined by the ratio of the hydrostatic stress, σ_m, to the Von Mises equivalent stress, σ_{eq}. The formulas for calculating σ_m and σ_{eq} are as follows:

$$\sigma_m = \frac{\sigma_1 + \sigma_2 + \sigma_3}{3} \tag{5}$$

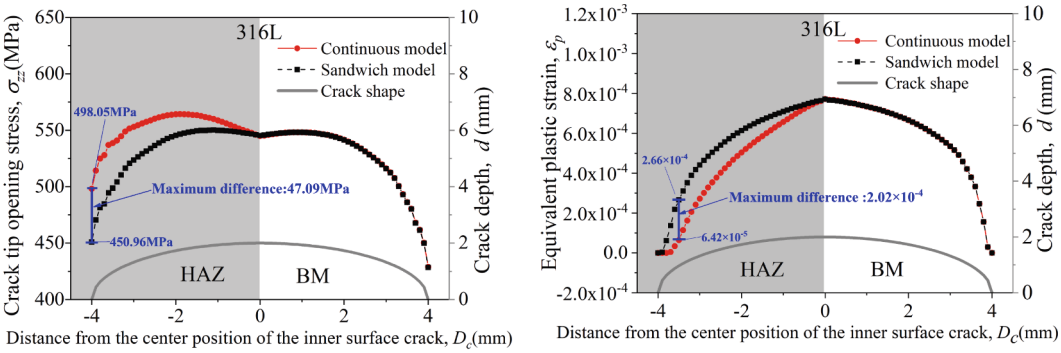

(a) Crack tip opening stress distribution (b) Equivalent plastic strain distribution

Fig. 17. Stress and strain distribution of internal surface cracks in 316L pipeline.

$$\sigma_{eq} = \sqrt{\frac{(\sigma_1 - \sigma_2)^2 + (\sigma_2 - \sigma_3)^2 + (\sigma_3 - \sigma_1)^2}{2}} \tag{6}$$

Where σ_1, σ_2, and σ_3 represent the principal stresses in different directions.

Fig. 18 presents a comparative analysis, revealing significant differences in the distribution of stress triaxiality at the crack tip between the sandwich model and the continuous transition model in DMWJ. Relative to the continuous transition model, the sandwich model overestimates the stress triaxiality at the crack tip front (i.e. 30 μm from the tip) by approximately 9%, 10%, and 6% in the HAZs of the SA508-52Mb interface (crack #1), 52Mw-316L interface (crack #2), and the 316L HAZ (crack #3), respectively. The results from both models exhibit a high degree of agreement in the BM region, where the material parameters are consistent. This observation confirms that the primary cause of the discrepancies at the interface is the variation in material mechanical properties across the welded joint.

It should be noted that the conservatism of the Sandwich Model warrants a nuanced discussion. While it underestimates the crack-

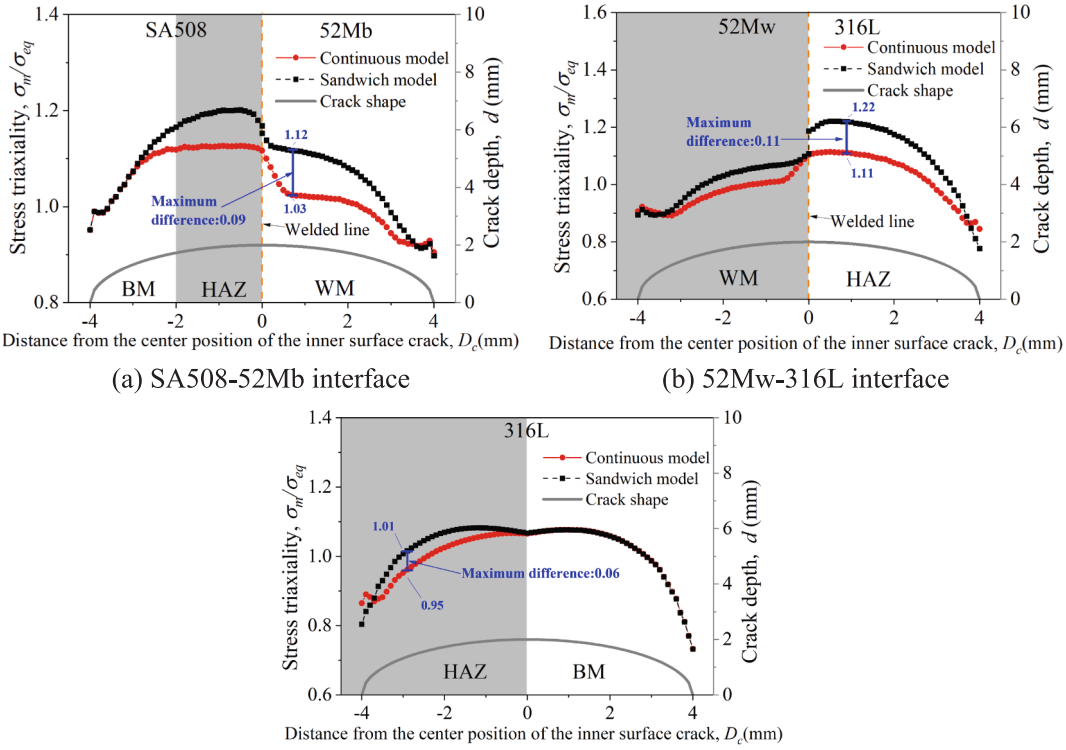

(a) SA508-52Mb interface (b) 52Mw-316L interface

(c) Location of 316L HAZ

Fig. 18. The distribution of three axis stress at the front edge of cracks in different locations.

tip opening stress (Figs. 13a, 15a and 17a), which could lead to non-conservative predictions in stress-driven assessments, it concurrently overestimates the stress triaxiality (Fig. 18a, b and c). Elevated stress triaxiality is known to reduce ductility and fracture resistance, implying that the model may yield conservative predictions with respect to constraint-sensitive failure mechanisms [34]. Consequently, the overall conservatism of the model is not unilateral but depends on the dominant failure mode in a given scenario, whether it is governed primarily by the local stress magnitude or by the triaxiality-induced loss of fracture toughness.

A comparative analysis of Figs. 13, 15, 17, and 18 indicates that the distribution of PEEQ correlates closely with the stress triaxiality pattern. Studies have shown that elevated stress triaxiality in the interfacial region of the welded joint reduces the plastic constraint capacity of the material near the crack tip. Meanwhile, the asymmetric plastic constraint capacity across the joint interface, which results from the lower constraint capability of low-strength materials, drives internal surface cracks to propagate preferentially toward directions with elevated crack-tip opening stresses. In the primary circuit welded joints of nuclear power safety ends, under conditions of fixed crack geometry and purely mechanical loading, interfacial internal surface cracks at the SA508-52Mb boundary exhibit a stronger tendency to propagate toward the HAZ of the SA508 BM, whereas those at the 52Mw-316L interface tend to propagate toward the HAZ of the 316L BM. Although the HAZ exhibits slightly lower stress triaxiality than the BM, the significantly higher crack-tip opening stresses within the HAZ dominate the crack propagation behavior, increasing the likelihood of crack growth through HAZ regions.

4.4. A comparative analysis of crack tip opening stress, PEEQ, and stress triaxiality across different locations

Under the condition of identical crack sizes, a comparative analysis was conducted on the crack tip opening stress, PEEQ, and stress triaxiality of inner surface axial cracks located at three different interfaces or zones: SA508-52Mb (Axial Crack #1), 52Mw-316L (Axial Crack #2), and the HAZ of the primary loop piping (Axial Crack #3), all obtained using the continuous transition model. Fig. 19(a), (b), and (c) illustrate the distributions of crack tip opening stress, PEEQ and stress triaxiality, respectively. As shown in Fig. 19(a), axial crack #1 exhibits the highest peak opening stress at the crack tip, whereas axial crack #3 shows the lowest, with axial crack #2 falling in between. Notably, the locations of maximum crack tip opening stress for all three inner surface cracks do not occur at the deepest point of the crack, but rather on both sides of the crack center.

The distribution of PEEQ at the crack tip, as shown in Fig. 19(b), differs from that of the crack tip opening stress. It can be observed that axial crack #3 exhibits the highest peak PEEQ at the crack tip, while axial crack #1 shows the lowest, with axial crack #2 again lying in between. This is attributed to the relatively lower plastic constraint capacity of materials with lower strength, which results in larger plastic strain occurring in such materials. Fig. 19(c) presents the distribution of stress triaxiality at the crack tip. For axial cracks

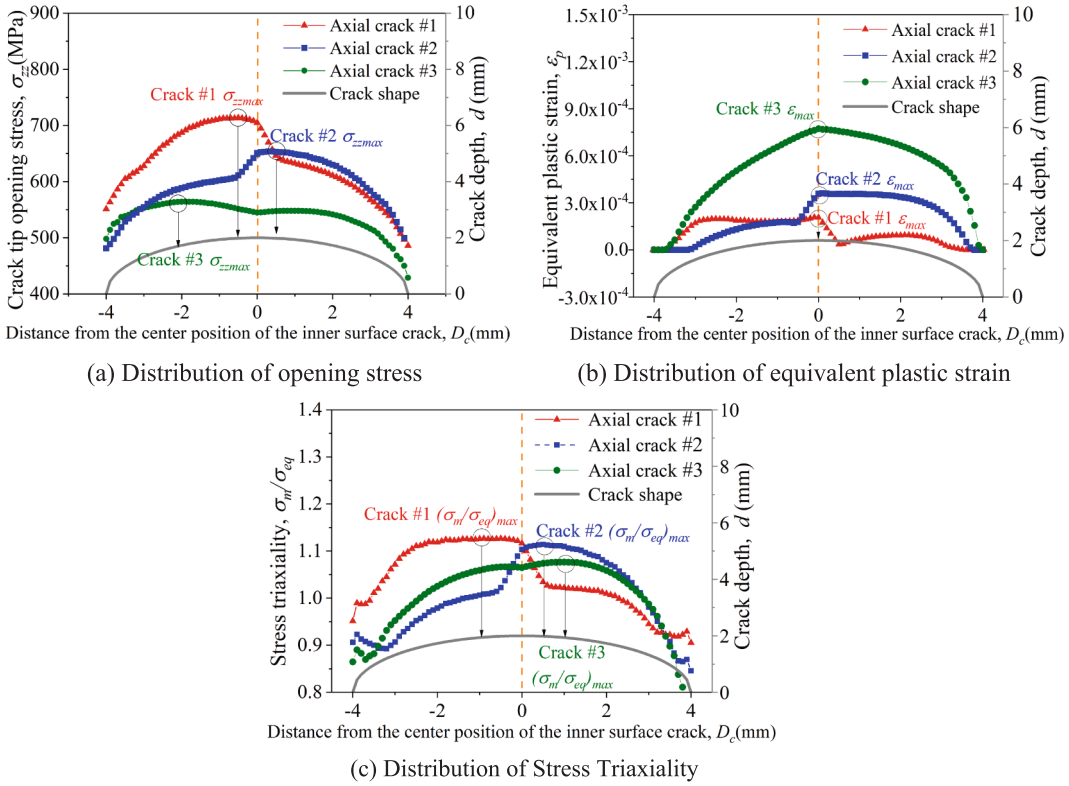

Fig. 19. Comparative analysis of opening stress, equivalent plastic strain, and stress triaxiality distributions at different locations.

#1 and #2, the variation in stress triaxiality closely resembles the trend observed in crack tip opening stress. However, for axial crack #3, the variation in stress triaxiality is opposite to that of the opening stress. Among the three, axial crack #3 exhibits the lowest peak stress triaxiality, while the peak stress triaxialities of axial cracks #1 and #2 are relatively close to each other.

5. Conclusion

In this study, a full-scale three-dimensional FE model of the DMWJ at the safe-end of a nuclear primary circuit was established via numerical simulation. The modeling process integrated the sub-modeling technique along with a predefined temperature field approach. The developed model systematically accounts for complex external loading conditions as well as the mechanical interactions arising from the heterogeneous material properties typical of DMWJs. An analysis was conducted on the distributions of stress, strain, and local stress triaxiality along the crack front under varying locations of internal surface cracks. Furthermore, based on the mechanical state along the crack tip, an assessment was carried out to evaluate potential crack propagation paths. The main conclusions are as follows:

(1) Significant mechanical heterogeneity exists in the welded joint due to an element dilution zone at the SA508-52Mb/52Mw-316L interface and high residual strains in the HAZ of both materials, which increases the likelihood of SCC in these regions.

(2) The sandwich model underestimates peak crack-tip opening stress by approximately 15% at the SA508-52Mb interface and 11% at the 52Mw-316L interface within their HAZs. Correspondingly, peak crack-tip PEEQ is overestimated by about 13% and 46%, while peak stress triaxiality is overestimated by roughly 9% and 10%, respectively.

(3) With the crack geometry fixed, results from the continuous transition model indicated that the maximum crack-tip opening stress and stress triaxiality were in the SA508 HAZ near the SA508-52Mb welded line, while the maximum PEEQ was at the 316L HAZ/BM interface.

(4) For an internal surface crack located at the SA508-52Mb interface, the analyzed mechanical fields suggest a higher driving force for propagation toward the SA508 HAZ. Similarly, cracks at the 52Mw-316L interface show a greater propensity to extend toward the 316L HAZ. This trend is also observed for cracks within the primary circuit piping, where the 316L HAZ presents a more critical mechanical environment.

By analyzing the mechanical inhomogeneity and crack-tip conditions of stationary inner surface cracks in DMWJs, this work establishes a foundational understanding of crack behavior. The critical aspects of crack initiation and propagation, essential for practical application, constitute the logical next phase of this research. It is noteworthy that accurately quantifying the crack driving force in future studies will require addressing the challenge posed by the severe property gradients across the DMWJ interface. For this strongly heterogeneous medium, employing path-independent numerical integration methods, such as the Equivalent Domain Integral (EDI) method, will be necessary to ensure the reliability of extracted fracture parameters.

CRediT authorship contribution statement

Shuai Wang: Writing – original draft, Visualization, Validation, Software, Funding acquisition, Data curation, Conceptualization. **Yapeng Li:** Writing – original draft, Software, Data curation. **Bin Wang:** Writing – review & editing, Supervision, Project administration, Funding acquisition, Conceptualization. **Wanzhong Li:** Software, Resources, Methodology, Formal analysis. **Lu Cui:** Supervision, Resources, Project administration, Formal analysis. **Guiyi Wu:** Writing – review & editing, Funding acquisition, Data curation. **Lorna Anguilano:** Software, Methodology, Formal analysis, Data curation. **He Xue:** Writing – review & editing, Funding acquisition, Conceptualization.

Declaration of competing interest

The authors declare that they have no known competing financial interests or personal relationships that could have appeared to influence the work reported in this paper.

Acknowledgements

This work was financially supported by the Xi'an Jiaotong University State Key Lab for Strength and Vibration for Mechanical Structures Open Lab Project, China (SV2023-KF-10); Royal Society, UK (IEC\NSFC\233524); National Natural Science Foundation of China (52275144); Scientific Research Program Funded by Shaanxi Provincial Education Department (25JP143); Shaanxi Provincial Key Research and Development Program, China (2025CY-YBXM-013).

Data availability

Data will be made available on request.

References

[1] Qiang B, Wang X. Ductile crack growth behaviors at different locations of a weld joint for an X80 pipeline steel: a numerical investigation using GTN models. Engng Fract Mech 2019;213:264–79. https://doi.org/10.1016/j.engfracmech.2019.04.009.

[2] Zhang S, Xue H, Wang S, Sun Y, Yang F, Zhang Y. Effect of mechanical heterogeneity on strain and stress fields at crack tips of SCC in dissimilar metal welded joints. Materials 2021;14(16):4450. https://doi.org/10.3390/ma14164450.
[3] Wang Z, Xue H, Hui Y, Wang R, Wu J, Zhang Y. Investigation of crack propagation and mechanical field evolution at the tip of a growing crack under variable loading in dissimilar metal welded joints. Int J Press Vessel Pip 2025;216:105496. https://doi.org/10.1016/j.ijpvp.2025.105496.
[4] Wang Z, Xue H, Wang R, Zhang Y. Effect of microstructure and mechanical heterogeneity on mechanical fields at stationary and growing crack tips in dissimilar metal welded joints. Adv Engng Mater 2025;27(10):2402868. https://doi.org/10.1002/adem.202402868.
[5] Wang Z, Xue Y, Wang R, Wu J, Zhang Y, Xue H. Review on crack growth driving force at the tip of stress corrosion cracking in the safe-end dissimilar metal welded joint. Nucl Engng Des 2024;429:113609. https://doi.org/10.1016/j.nucengdes.2024.113609.
[6] Wang Z, Xue H, Wang S, Zhang Y. A multi-method coupled approach to simulate crack growth path and stress-strain field at the tip of the growing crack in the dissimilar metal welded joint. Int J Press Vessel Pip 2023;206:105046. https://doi.org/10.1016/j.ijpvp.2023.105046.
[7] Bi Y, Yuan X, Lv J, Bashir R, Wang S, Xue H. Effect of yield strength distribution welded joint on crack propagation path and crack mechanical tip field. Materials 2021;14(17):4947. https://doi.org/10.3390/ma14174947.
[8] Gong N, Wang GZ, Xuan FZ, Tu ST. Leak-before-break analysis of a dissimilar metal welded joint for connecting pipe-nozzle in nuclear power plants. Nucl Engng Des 2013;255:1–8. https://doi.org/10.1016/j.nucengdes.2012.09.030.
[9] Zhao L, Yang B, Sun Y. Crack-tip constraint analysis of the dissimilar metal-welded joint and constraint match with test specimens. Nucl Sci Engng 2025;199:1512–27. https://doi.org/10.1080/00295639.2025.2456369.
[10] Gu S, Wu J, Wang X, Cui W, Yang J, Chen H. Effect of residual stress introduced by local loading on fracture behaviour of DMWJ under different constraints. Int J Press Vessel Pip 2023;202:104885. https://doi.org/10.1016/j.ijpvp.2023.104885.
[11] Okonkwo BO, Ming H, Wang J, Meng F, Xu X, Han EH. Microstructural characterization of low alloy steel A508–309/308L stainless steel dissimilar weld metals. Int J Press Vessel Pip 2021;190:104297. https://doi.org/10.1016/j.ijpvp.2020.104297.
[12] Dong L, Zhang X, Han Y, Peng Q, Deng P, Wang S. Effect of surface treatments on microstructure and stress corrosion cracking behavior of 308L weld metal in a primary pressurized water reactor environment. Corros Sci 2020;166:108465. https://doi.org/10.1016/j.corsci.2020.108465.
[13] Dong L, Zhang Y, Han Y, Peng Q, Han EH. Environmentally assisted cracking in the fusion boundary region of a SA508-Alloy 52M dissimilar weld joint in simulated primary pressurized water reactor environments. Corros Sci 2021;190:109668. https://doi.org/10.1016/j.corsci.2021.109668.
[14] Wang S, Wang B, Janin YJ, Bourga R, Xue H. Effects of the surface crack shape on J values along the front of an elliptical crack. Fatigue Fracture Eng Mater Struct 2021;44(11):2944–61. https://doi.org/10.1111/ffe.13522.
[15] Peng D, Huang P, Jones R, Bowler A, Edwards D. A simple method based for computing crack shapes. Engng Fail Anal 2016;59:41–56. https://doi.org/10.1016/j.engfailanal.2015.11.016.
[16] Xue H, Sato Y, Shoji T. Quantitative estimation of the growth of environmentally assisted cracks at flaws in light water reactor components. J Press Vessel Technol-Trans ASME 2009;131(1):011404. https://doi.org/10.1115/1.3027458.
[17] Wang S, Xue H, Wu G, Wang Z, Zhao K, Ni C. Investigation of the inhomogeneous mechanical and crack driving force of low alloy steel SA508 and its Welded 309L/308L stainless steel cladding. Nucl Sci Engng 2023;197(4):623–32. https://doi.org/10.1080/00295639.2022.2123210.
[18] GB/T 22458-2008, General rules of instrumented nanoindentation test, Standardization Administration of China, China Quality and Standards Publishing and Media Company Limited (2012). Retrieved from https://openstd.samr.gov.cn/bzgk/gb/newGbInfo?hcno=D41A27970B0503F50A414F4D519B0DD0.
[19] Wang S. Study on the effect of material inhomogeneity on mechanical state at crack tip of the safety end welded joint in nuclear power plant (Doctoral dissertation). Xi'an Univ Sci Technol 2021. https://doi.org/10.27397/d.cnki.gxaku.2021.001052.
[20] Fan K. Study on local fracture behavior of materials interface regions in dissimilar metal welded joints in nuclear power plant. East China University of Science and Technology; 2018. Doctoral dissertation.
[21] De Beule M, Mortier P, Belis J, Van Impe R, Verhegghe B, Verdonck P. Plasticity as a lifesaver in the design of cardiovascular stents. Key Engng Mater 2007;340:841–6. https://doi.org/10.4028/www.scientific.net/KEM.340-341.841.
[22] Wang HT, Wang GZ, Xuan FZ, Liu CJ, Tu ST. Local mechanical properties of a dissimilar metal welded joint in nuclear power systems. Mater Sci Engng A 2013;568:108–17. https://doi.org/10.1016/j.msea.2013.01.037.
[23] Xue H, Wang Z, Wang S, He J, Yang H. Characterization of mechanical heterogeneity in dissimilar metal welded joints. Materials 2021;14(15):4145. https://doi.org/10.3390/ma14154145.
[24] Wang HT, Wang GZ, Xuan FZ, Tu ST. An experimental investigation of local fracture resistance and crack growth paths in a dissimilar metal welded joint. Mater Des 2013;44:179–89. https://doi.org/10.1016/j.matdes.2012.07.067.
[25] Wang HT, Wang GZ, Xuan FZ, Tu ST. Fracture mechanism of a dissimilar metal welded joint in nuclear power plant. Engng Fail Anal 2013;28:134–48. https://doi.org/10.1016/j.engfailanal.2012.10.005.
[26] Liu ZW. Study on the defect assessment methods for the dissimilar weld joint in the Safe-end of the AP1000 Nuclear pressure Vessel (Master's thesis). East China University of Science and Technology; 2011.
[27] Xue H, Gui YK, Wang WB, Li XB, Wang YR, Tao XQ, et al. Effect of a single overload on the fracture behavior in safe-end dissimilar metal welded joints in nuclear power plant. Adv Mat Res 2014;1049:600–4. https://doi.org/10.4028/www.scientific.net/AMR.1049-1050.600.
[28] Ha T, Murudkar R, Hartwig KT, Welo T, Ringen G, Wang J. A feasibility study of continuous grain refinement of sheet metal. Procedia Manuf 2020;48:379–87. https://doi.org/10.1016/j.promfg.2020.05.060.
[29] Hou Z, Xiu S, Yao Y, Sun C. The residual stress and martensitic transformation of 304 stainless steel in pre-stress grinding: influence and control on chloride induced SCC. J Mater Res Technol 2023;24:4601–17. https://doi.org/10.1016/j.jmrt.2023.04.096.
[30] Zhang W, Wang X, Wang S, Wu H, Yang C, Hu Y, et al. Combined effects of machining-induced residual stress and external load on SCC initiation and early propagation of 316 stainless steel in high temperature high pressure water. Corros Sci 2021;190:109644. https://doi.org/10.1016/j.corsci.2021.109644.
[31] Ford FP, Andresen P L. Development and use of a predictive model of crack propagation in 304/316L, A533B/A508, and inconel 600/182 alloys in 2880℃ water. In: Theus GJ, Weeks J R. Proc. 3rd Int. Symp. on environmental degradation of Mats. In Nucl. power systems-water reactors. Warrendale, PA, USA: TMS, 1988:789-800.
[32] Ford FP, Andresen PL, Solomon H, et al. Application of water chemistry control, on-Line monitoring and crack growth rate models for improved BWR material performance. In: Cubicciotti D. Proc. 4th Int. Symp. on environmental degradation of Mats. in Nucl. Power Systems-Water Reactors. Houston: NACE, 1989:4-26 to 4-50.
[33] Ford FP. Quantitative prediction of environmentally assisted cracking. Corrosion: J Sci Eng 1996;52(5):375–95. https://doi.org/10.5006/1.3292125.
[34] Yoo SC, Choi KJ, Kim T, et al. Effects of thermal aging and stress triaxiality on PWSCC initiation susceptibility of nickel-based Alloy 600. J Mech Sci Technol 2016;30(10):4403–6. https://doi.org/10.1007/s12206-016-0901-3.